New Journal of Physics
The open-access journal for physics

Two-photon quantum walks in an elliptical direct-write waveguide array

J O Owens[1], M A Broome[1,5], D N Biggerstaff[1], M E Goggin[1,2], A Fedrizzi[1], T Linjordet[3], M Ams[4], G D Marshall[4], J Twamley[3], M J Withford[4] and A G White[1]

[1] ARC Centre for Engineered Quantum Systems, ARC Centre for Quantum Computer and Communication Technology, School of Mathematics and Physics, University of Queensland, Brisbane, QLD 4072, Australia
[2] Department of Physics, Truman State University, Kirksville, MO 63501, USA
[3] ARC Centre for Engineered Quantum Systems, Department of Physics and Astronomy, Macquarie University, North Ryde, NSW 2109, Australia
[4] ARC Centre for Ultrahigh Bandwidth Devices for Optical Systems, Centre for Quantum Science and Technology, MQ Photonics Research Centre, Department of Physics and Astronomy, Macquarie University, North Ryde, NSW 2109, Australia
E-mail: m.a.broome@googlemail.com

New Journal of Physics **13** (2011) 075003 (13pp)
Received 25 February 2011
Published 13 July 2011
Online at http://www.njp.org/
doi:10.1088/1367-2630/13/7/075003

Abstract. Integrated optics provides an ideal testbed for the emulation of quantum systems via continuous-time quantum walks. Here, we study the evolution of two-photon states in an elliptic array of waveguides. We characterize the photonic chip via coherent light tomography and use the results to predict distinct differences between temporally indistinguishable and distinguishable two-photon inputs, which we then compare with experimental observations. This work highlights the feasibility of emulation of coherent quantum phenomena in three-dimensional waveguide structures.

[5] Author to whom any correspondence should be addressed.

Contents

1. Introduction

Computer modelling of complex systems has contributed greatly to modern science owing to sophisticated approximation methods and steadily increasing computational power. However, classical simulation methods are ultimately impractical for modelling even moderately sized quantum systems due to an exponentially increasing parameter space. As first proposed by Feynman [1], a possible solution is for the model itself to operate via quantum instead of classical dynamics, either through *simulation*, in which a digital model on a quantum computer yields physical quantities as in e.g. [2–4], or through *emulation*, in which a quantum system is modelled by a better-controllable system with a sufficiently similar Hamiltonian.

Quantum walks [5, 6]—an extension of the classical random walk into the quantum world—provide an ideal framework for emulation due to their rich dynamics [7–9]. There are two limiting cases, discrete and continuous. In discrete-time quantum walks, one or more (interacting) quantum particles (the so-called quantum coin) evolve on a graph, with their evolution governed by their internal quantum (coin) states. The discrete-time quantum walk on a line is the best-studied example of such a walk and it has been demonstrated in a number of physical systems [10–14].

In continuous-time quantum walks, in contrast, there are no coin operations and the evolution is defined entirely in position space [15]. These walks require a well-controlled, continuous coupling between vertices or lattice sites. Integrated optics is perfectly suited for this task, and lithographically written, evanescently coupled surface waveguides were the first system used to demonstrate a quantum walk on a line with coherent light [16]. Unfortunately, surface waveguides can only realize simple, one-dimensional (1D) graphs with limited interconnectivity.

Physically more interesting 3D structures can be engineered in laser-written optical waveguide arrays in dielectric materials such as fused silica [17, 18], a platform that has been shown to have suitable fidelity for photonic quantum information processing [19]. The 2D graphs that can be realized with this technique allow the study of new quantum walk phenomena, such as wave communication [20], cooperative quantum games [21] and the creation of topological phases in 2D [22]. Examples of direct-write waveguide array structures relevant to these problems include rings, hexagonal lattices, X-shapes and triangular shapes [23–25]. To date, however, these have only been explored with classical light inputs, and specifically in the context of 2D quantum walks in [25]. True quantum effects, and genuine efficiency

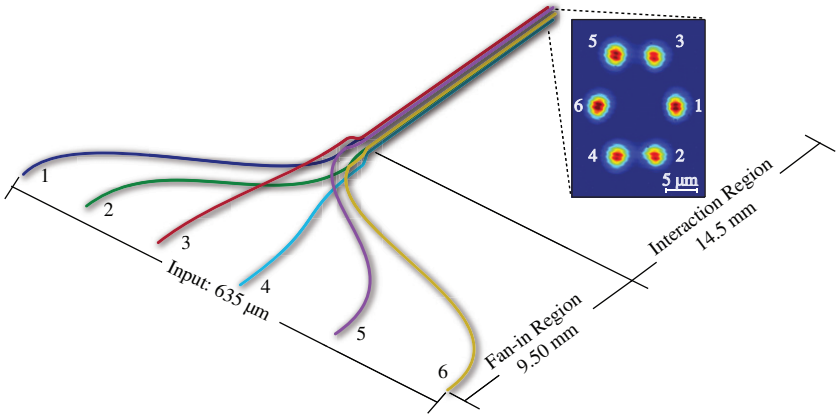

Figure 1. Schematic representation of the integrated waveguide circuit (drawing not-to-scale) and associated output. At the input the waveguides are equally spaced by 127 μm. They then converge via a two-stage fan-in to their eventual elliptical configuration. The inset is a CCD image of the output: the waveguides are arranged with equal angular spacing around an ellipse with semi-major and semi-minor radii of 10.2 and 7.0 μm, respectively.

improvements in emulating quantum systems, will only emerge for non-classical input states as pointed out (for discrete-time walks) in [26]. The first such walk in the continuous regime was recently demonstrated in a linear waveguide array with two-photon inputs in [27].

Here, we study multi-walker continuous-time 2D quantum walks in an optical chip containing an elliptical arrangement of coupled direct-write waveguides. We characterize the optical chip via coherent light tomography, effectively realizing single-particle walks and use the results to predict correlations for non-classical two-photon walks that we compare with experimental observations. This work is an important step towards the emulation of quantum systems in 3D integrated photonic architectures.

2. Device description

The circuit for the quantum walk, shown in figure 1, consists of six waveguides written into a chip of high-purity fused silica using an ultrafast direct-write technique, described in detail in [19]. In this technique, femtosecond Ti : sapphire laser pulses tightly focused inside the sample yield localized refractive index modifications. The sample is translated in all dimensions to create true 3D curved waveguides, a process that cannot be replicated by conventional lithographic techniques. Our chip was written with a 1 kHz repetition rate, 800 nm, 120 fs laser, passed through a 520 μm slit and focused with a 40×0.6 NA microscope objective. The maximum refractive index difference between the waveguides and the substrate is approximately $\Delta n \sim 0.0062$.

At the input, the six waveguides are arranged in a line with equal spacing of 127 μm, allowing each waveguide to be addressed individually and simultaneously. The waveguides converge via a two-stage fan-in to their final configuration as shown in figure 1. In the primary fan-in stage, which occupies the first ~ 8.5 mm of the chip, the waveguides follow S-bend curves from a linear input arrangement to an elliptical configuration twice as large in radius as their

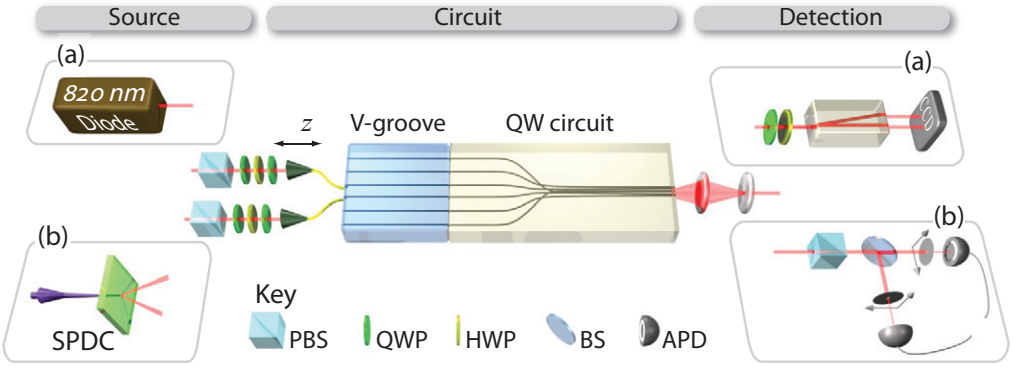

Figure 2. Experimental setup. The chip can be addressed with six individual single-mode fibres. The input light polarization is set by a combination of half- and quarter-wave plates (HWP and QWP) and polarizing beamsplitters (PBS). The chip output is magnified and then collimated with two spherical lenses. (a) The chip was characterized with an 820 nm laser diode, imaged onto a CCD camera via a polarizing prism. (b) Quantum walks were performed with two-photon inputs created via spontaneous parametric downconversion (SPDC). The relative delay Δz between the two input photons was adjusted using a translation stage. We used a 50/50 beamsplitter (BS) and two $\sim 500\,\mu$m apertures to select a combination of output ports and measure the two-photon correlations in coincidence using single-photon avalanche diodes.

final configuration. In the second fan-in stage, during the next 1 mm, further S-bends shrink this ellipse to have a semi-major axis of 10.2 μm and a semi-minor axis of 7.0 μm. Studying an elliptical array provides additional insights into the coupling between waveguides as this shape breaks the degeneracy of the inter-waveguide distance. The expected inter-waveguide coupling constants are given in the appendix; notably some of the next-nearest-neighbour and even next-next-nearest-neighbour couplings are non-negligible over the interaction length in the chip. All the S-bends are of the 'raised-sine' form, which has been shown to minimize bend loss [28], while the two-stage fan-in configuration was designed to minimize coupling (in particular, *asymmetrical* coupling) between waveguides before they attain their final interaction configuration.

The light evolution in this array is governed by the evanescent inter-waveguide coupling, which drops off exponentially as a function of the waveguide distance. As an approximation, it can be theoretically described by a coupled-oscillator Hamiltonian; see the appendix.

3. Optical chip characterization

The experimental setup is shown in figure 2. Light was coupled into the chip via a V-groove array, which houses six single-mode optical fibres on a line, matching the input spacing of the circuit waveguides. We first illuminated individual waveguides in the chip using coherent light from an 820 nm laser diode; see figure 2(a). The output intensity profiles were processed in Matlab and converted into probability distributions. Compared to the numerical simulation obtained with the software suite used to design the chip, the observed distribution at the

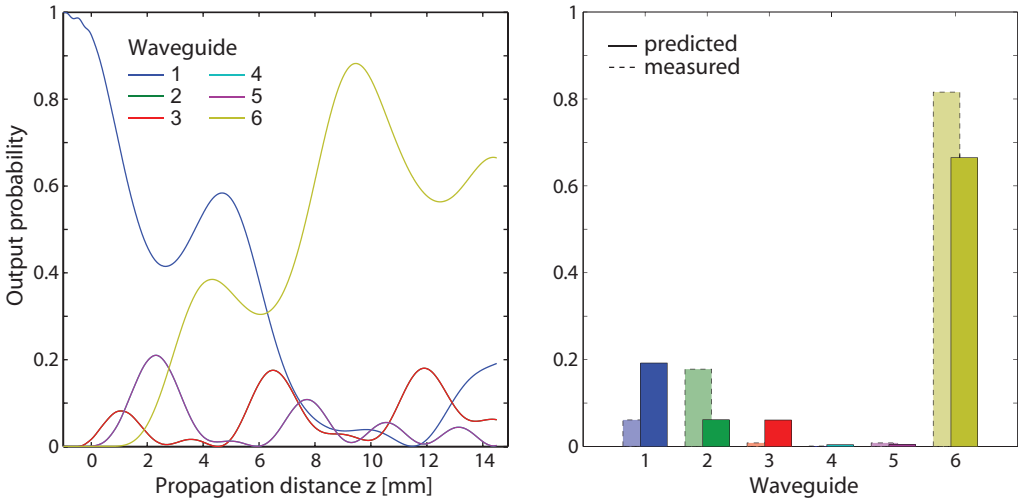

Figure 3. Comparison of numerical simulations and observed probability distributions for the optical chip in figure 1(a). The propagation dynamics predicted using optical waveguide simulation software (see the appendix) with light input into waveguide 1, as a function of z. The simulation includes modelling of inter-waveguide coupling during the 1 mm second fan-in stage at $z \leqslant 0$. The curves for waveguides 2 and 3, and 4 and 5 overlap due to symmetry. (b) The predicted distribution at the output of the circuit, and the corresponding observed probabilities. The asymmetry in the measured distribution indicates that the optical response of the chip is not scalar, instead suggesting some vectorial behaviour. This was confirmed by further tomographic analysis.

circuit output differed significantly; see figure 3. This behaviour prompted us to empirically determine the full optical response of the circuit using polarization-sensitive, coherent light tomography.

For this tomography, the input polarization was set using a bare reference fibre on top of the chip. Into each waveguide we input the following set of polarization states: $\{|H\rangle, |V\rangle, |D\rangle, |A\rangle, |L\rangle, |R\rangle\}$, where $|H\rangle$ and $|V\rangle$ represent horizontal and vertical polarization and $|D/A\rangle = (|H\rangle \pm |V\rangle)/\sqrt{2}$, $|L/R\rangle = (|H\rangle \pm \mathrm{i}\,|V\rangle)/\sqrt{2}$. For each output we measured the same six polarizations components, obtaining a total of 216 CCD images.

Using output intensity distributions taken from these images, we subsequently reconstructed an array of 36 Mueller matrices $\mathcal{M}$ [29]. This array completely characterizes the optical response of the circuit, quantifying the effects of three distinct processes: notably polarization-dependent inter-waveguide coupling, birefringence and polarization-dependent loss [29].

The results indicate strong birefringence in each of the six waveguides. Most notably, when the state $|H\rangle$ is input into waveguide 5, 29% of the overall output state across the six channels is rotated to $|V\rangle$. For input channels 1, 2 and 4, the overall polarization rotation was small, with more than 91% of $|H\rangle$ being retained at the output. Furthermore, there was significant polarization-dependent coupling between the waveguides for all input channels. For instance, for input $|H\rangle$ into waveguide 1, 80% of the total output intensity was observed in channel 6; however, when the input state was $|V\rangle$, only 11% of the total output intensity was contained

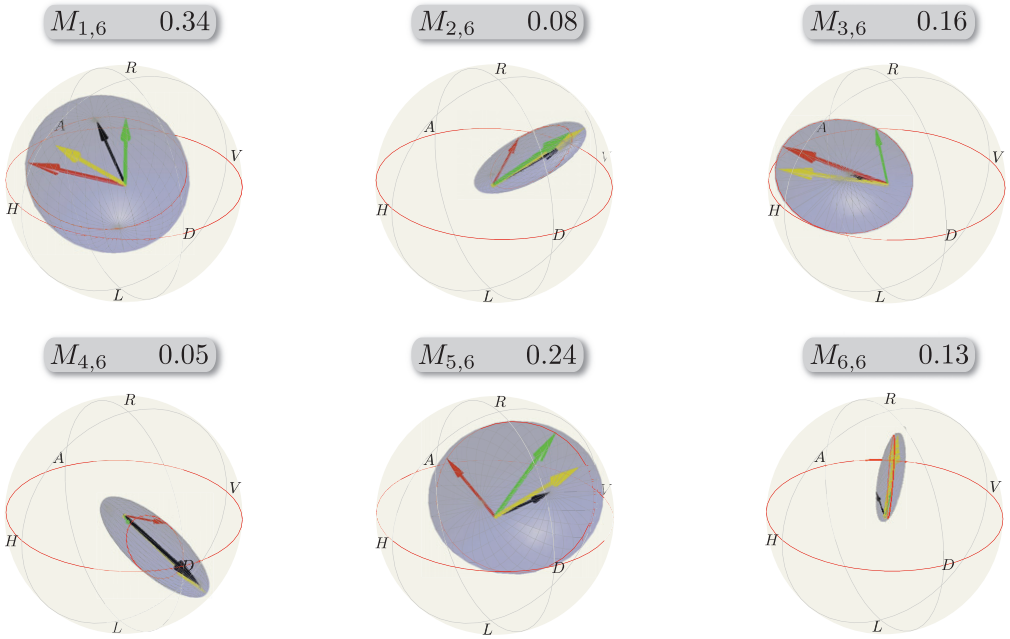

Figure 4. Poincaré sphere representation of the corresponding Mueller matrices, $M_{\text{out,in}}$ (see the appendix), describing the transformation from input waveguide 6 to outputs 1–6. Input states shown on the outer Poincaré spheres are mapped to different locations on the blue ellipsoids, simultaneously showing polarization-dependent coupling and birefringent effects in the respective channel. The relative orientation of the ellipsoids is indicated by the set of orthogonal states $|H\rangle$ (red arrow), $|D\rangle$ (green arrow) and $|R\rangle$ (black arrow), and the point of contact between the sphere and the ellipsoid is indicated by the yellow arrow. Note that the arrow lengths are proportional to output power, *not* degree of polarization. The numbers above each sphere give the normalized average power coupled into the respective channel.

in this channel. An exemplary selection of Mueller matrices, illustrated on Poincaré spheres and quantifying these effects, is shown in figure 4. The full matrix array $\mathcal{M}$ can be found in the appendix.

In addition, the whole chip exhibited significant polarization-dependent loss; integrating over all output channels, we observed an excess 38% loss of $|V\rangle$ compared with $|H\rangle$ for waveguide 6. This may be due to a combination of absorption into the bulk of the circuit or polarization dependence of the input coupling efficiency from the V-groove array to the chip or both.

4. Two-photon walks

The coherent light tomography encompasses all possible single-photon walks in this chip, since a single photon shares the coherence properties of a coherent light beam. However, these walks can be efficiently simulated classically and it is not until we input multi-photon states that we observe quantum effects [26].

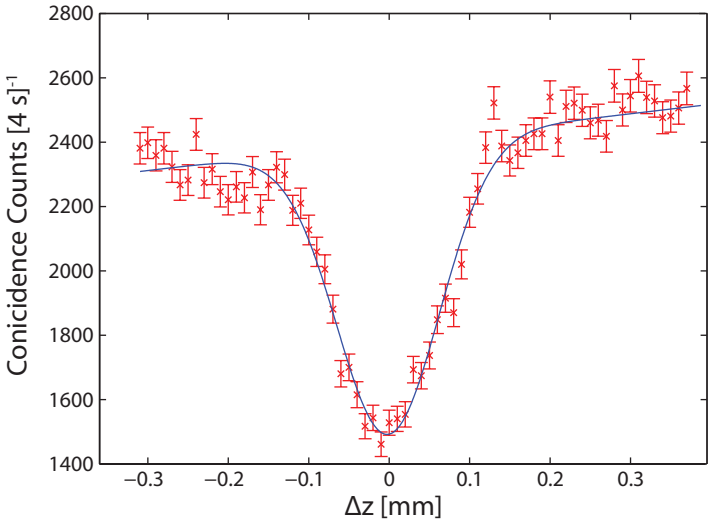

Figure 5. Example of observed two-photon interference between output waveguides 2 and 6 as a function of relative path difference between photon pairs input into neighbouring waveguides 1 and 2. The visibility of the dip is $\mathcal{V}_{2,6} = 38 \pm 2\%$, calculated from a Gaussian fit (blue line).

A schematic representation of the setup for the two-photon walk experiment is shown in figure 2(b). Pairs of single photons are created via spontaneous parametric down-conversion: a mode-locked 76 MHz laser centred at 820 nm is frequency doubled to 410 nm and focused into a 2 mm-long β-barium borate (BBO) crystal, phase-matched for type-I downconversion. After passing through interference filters at 820 ± 2.5 nm, the degenerate photon pairs are coupled into single-mode fibres equipped with manual polarization controllers. Photons are coupled into the chip via the V-groove fibre array.

We created photon pairs at a rate of 180 kHz, of which we detected a total of 6.5 kHz at the circuit output. The single-photon loss is thus $\sim 73\%$, factoring out the 50/50 beamsplitter, which reduces the number of coincidences by 50%. The main loss contributions stemmed from the poor input coupling efficiency between the V-groove array and the chip ($\sim 31\%$). The imperfect coupling is mostly due to a slight mismatch between the spacing of the fibres in the V-groove array and the locations of the input ports of the circuit. Intrinsic waveguide loss was negligible in comparison. The observed loss could be significantly reduced by using a more sophisticated imaging system.

We carried out two-photon quantum walks in two separate scenarios: with temporally distinguishable and indistinguishable photons. When the photons entering the chip are temporally distinguishable, i.e. with a time delay larger than their respective coherence times, they perform independent quantum walks with local evolution. When they enter the chip simultaneously, $\Delta z = 0$, they experience non-classical two-photon interference [30], yielding quantum dynamics, including the generation of two-photon entanglement. The theoretic qualitative difference between these two cases is described in the appendix. Figure 5 shows an exemplary calibration scan of coincidence counts as a function of temporal delay. The signature of indistinguishable quantum walkers manifests as a dip in the rate of coincident detection events, C, at zero delay, with an interference visibility of $\mathcal{V} = (C_{\max} - C_{\min})/C_{\max}$ of $38 \pm 2\%$.

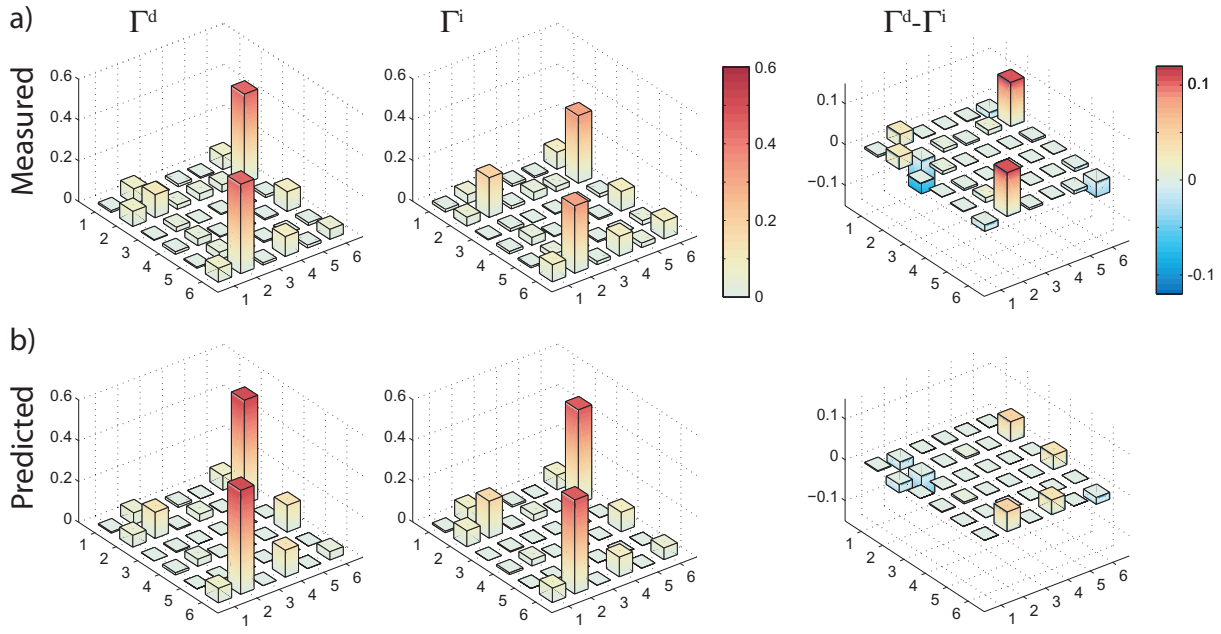

Figure 6. Correlation matrices for nearest-neighbour input channels 1 and 2. We recorded the photon-coincidence counts at each of the 36 pairs of output channels in a 20 s time window. (a) The measured and (b) predicted correlation matrices for (left) temporally distinguishable photon pairs Γ^d, (center) temporally indistinguishable simultaneous walkers Γ^i and (right) the difference $\Gamma^d - \Gamma^i$. The coincidence probability at outputs 2 and 6 between the two plots reflects the two-photon interference dip shown in figure 5. The measured uncertainties are not plotted, as they are too small to be seen on the plots.

The results on two-photon quantum walks for distinguishable and indistinguishable photons input into the *nearest*-neighbour channels 1 and 2 are shown in figure 6(a), as the normalized coincidence probability distributions, Γ^d and Γ^i, respectively. Distinct differences are observed between the two cases, as suggested by the strong two-photon interference signature in figure 5.

The measured distributions are compared with predictions, figure 6(b), which are based on determining the components of the waveguide array unitary U, for a particular input polarization; see the appendix for details. The generalized overlap fidelities S, defined in the appendix, between our measurements and predictions are $S^{\mathrm{d}} = 93.4 \pm 0.3\%$ for the distinguishable walkers and $S^{\mathrm{i}} = 91.6 \pm 0.4\%$ for the indistinguishable walkers.

Figure 7(a) shows correlation matrices for inputs 2 and 4 as an example of two-photon walks with *next*-nearest neighbour input ports. We again observe non-classical interference signatures, with visibilities up to $\mathcal{V}_{2,4} = 28 \pm 3\%$. The fidelities between the measured two-photon matrices and their corresponding predictions, figure 7(b), are $S^{\mathrm{d}} = 97.9 \pm 1\%$ and $S^{\mathrm{i}} = 96.2 \pm 0.8\%$.

5. Discussion

In conclusion, we have performed the first quantum walk in a 3D waveguide structure with genuine non-classical inputs. This is a significant step towards emulating Hamiltonians, which

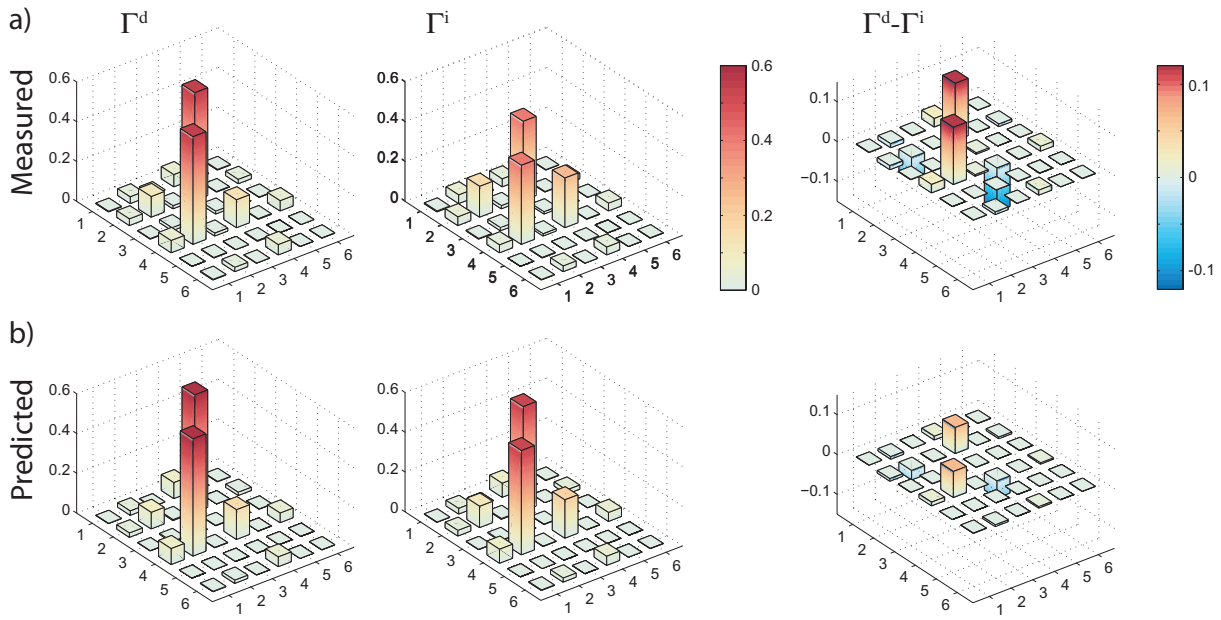

Figure 7. Correlation matrices for next-nearest neighbour input channels 2 and 4. The plots follow the same convention as those in figure 6, for both (a) the measured and (b) predicted correlation matrices. Uncertainties are again too small to be seen on the graphs.

can be approximated by evanescently coupled waveguides. However, we have also identified a number of obstacles that must be addressed before such an approach can be fully realized.

Firstly, despite the apparent good agreement between our predictions and the observed two-photon probability distributions, the two-photon visibilities—which quantify the measured non-classical effects—matched the predictions poorly. This is because the Mueller-matrix array derived from the coherent beam intensities only yields the squared absolute values of the elements of the system's unitary U; it does not determine the (generally complex) phase relations of the waveguide array. These phase factors could in principle be obtained by phase-sensitive coherent light tomography, as proposed in [25, 31]. An alternative technique [32] requires a single N-photon input state (in this case $N = 6$) and photon-number resolved detection at each output. However, generating Fock states is hard and both techniques suffer from the large number of measurements required to fully characterize the six-port system. This is a perennial problem in quantum science: the exponential power granted by multi-photon walks on big lattices makes it hard to experimentally characterize system dynamics. A potential solution might be to use compressive sensing techniques, which have recently been exploited for exponentially efficient quantum process tomography [33].

Secondly, while we observed significant two-photon interference visibilities, the resulting probability distributions did not exhibit a conclusively quantum signature, as quantified by the witness defined in [16]. This was most likely due to the significant polarization-dependent coupling and loss in the circuit, leading to non-unitary evolution, which failed to preserve the coherence of the input quantum state. With a better understanding of the origins and mechanisms of these effects, they could be exploited to engineer devices such as polarization-dependent

couplers. It should be noted that these effects are certainly not inherent to the direct-write technique, as demonstrated by for example [34].

Future research should also focus on realizing decoherence in continuous-time walks. Many physical, biological or chemical systems are strongly coupled to their environment and decoherence has been suggested to be the driving factor behind phenomena such as environmentally assisted quantum transport [9]. While decoherence has been studied in discrete-time experiments [14], techniques for controllably introducing it into inherently robust waveguide lattices are yet to be demonstrated.

The emulation of classically intractable physics requires scaling up to larger, more elaborate waveguide structures, which is certainly feasible, as demonstrated in [23–25]. However, it will be tricky to address the individual modes in these systems, as the fan-in we demonstrate in our paper has its limitations. The theory will also have to catch up; unlike for quantum simulation, there are no known fault-tolerance or error-correction techniques for quantum emulation in quantum walks.

Acknowledgments

We thank I Kassal, B P Lanyon, G G Gillett, J C F Matthews and J L O'Brien for valuable assistance. We acknowledge financial support from Australian Research Council Centres of Excellence, Discovery and Federation Fellow programs and an IARPA-funded US Army Research Office contract.

Appendix

In the Heisenberg picture, a light field input into a waveguide in this chip is subject to the coupled-oscillator Hamiltonian [16]

$$H = \sum_{i=1}^{6} \beta_i a_i^\dagger a_i + \sum_{i,j=1}^{6} C_{i,j} a_i^\dagger a_j, \tag{A.1}$$

where β_i is the propagation constant in waveguide i and $C_{i,j}$ is the coupling constant between waveguides i and j. The system then evolves in time according to the unitary operator $U(t) = \mathrm{e}^{-\mathrm{i}Ht/\hbar}$ and the creation operators $a_i^\dagger$ are subject to the Heisenberg equation of motion

$$\frac{\partial a_i^\dagger}{\partial z} = \frac{n}{c}\frac{\partial a_i^\dagger}{\partial t} = \mathrm{i}\left[H, a_i^\dagger\right] = \mathrm{i}\beta a_i^\dagger + \mathrm{i}\sum_{j=1}^{6} C_{i,j} a_j^\dagger, \tag{A.2}$$

which has the solution

$$a_i^\dagger(z) = \sum_j (\mathrm{e}^{\mathrm{i}zC})_{i,j} a_j^\dagger(0) = \sum_j U_{i,j}(z) a_j^\dagger(0), \tag{A.3}$$

where $C = \{C_{i,j}\}$ is the 6×6 matrix of coupling constants with diagonal entries $C_{i,i} = \beta$, and z is the propagation distance along the waveguide array. Note that this evolution is equivalent to the continuous-time quantum walk formalism [15].

The interaction length z of the waveguides is chosen to match the desired run time t for the emulation of the Hamiltonian. The overall response of the circuit as a 12-port beam-splitting device is then contained in the unitary matrix $U = \mathrm{e}^{\mathrm{i}zC}$, and we can define a set of six output creation operators $b_i^\dagger$, with $b_i^\dagger = a_i^\dagger(z) = \sum_j U_{i,j} a_j^\dagger$ for the input operators $a_j = a_j(0)$.

The coupling $C_{i,j}$ between two waveguides falls off exponentially with waveguide separation $r_{i,j}$ [23], so to design an array of the type discussed in this paper, the number of waveguides, their geometry, and their separations $r_{i,j}$ are chosen to reflect the properties of the Hamiltonian under investigation. This determines the parameters β_i and $C_{i,j}$. An interaction length z is chosen according to the desired emulation time t.

To translate the theoretical design into a real experimental system, the geometry of the circuit is analysed in a numerical electromagnetic design suite, in our case *RSoft* (http://www.rsoftdesign.com/). This program uses finite-difference algorithms to find solutions to Maxwell's equations in dielectrics and can be used to optimize a set of physical parameters (core diameter and refractive index contrast) that will approximate the desired evolution. This provides the link between the Hamiltonian evolution of the quantum system under study and the physical properties of the experimental system. For our chip, simulation predicts two leading nearest-neighbour coupling strengths of $C_{24} = 0.963\,\mathrm{mm}^{-1}$ and $C_{12} = 0.312\,\mathrm{mm}^{-1}$, reflecting the elliptical geometry. The next-nearest neighbour and further coupling values are $C_{14} = 0.050\,\mathrm{mm}^{-1}$, $C_{16} = 0.044\,\mathrm{mm}^{-1}$, $C_{23} = 0.009\,\mathrm{mm}^{-1}$ and $C_{25} = 0.005\,\mathrm{mm}^{-1}$. The latter two are negligible: our model predicts that, in the absence of the other waveguides, less than 2% of light input into one waveguide of either of these pairs would couple to the other waveguide over the interaction length of the chip. However, the next-nearest neighbour coupling C_{14} and even the next-next-nearest neighbour coupling C_{16} are notably *non*-negligible, respectively, leading to modelled values of 40% and 33% coupling between these waveguide pairs, in the absence of all other waveguides, over the interaction length of the chip.

We now describe the two-photon evolution in the optical system. Two temporally indistinguishable input photons $|\Psi\rangle = a_i^\dagger a_j^\dagger |0\rangle$, for $i \neq j$, give the joint detection probability $\Gamma^i_{k,l}$ of finding the state $b_k^\dagger b_l^\dagger |0\rangle$ in output modes k and l [16]:

$$\Gamma^i_{k,l} = \langle b_l^\dagger b_k^\dagger b_k b_l \rangle_\Psi = \frac{1}{1+\delta_{k,l}} |U_{i,k}U_{j,l} + U_{j,k}U_{i,l}|^2. \tag{A.4}$$

The matrix $\Gamma^i = \{\Gamma^i_{k,l}\}$ then describes the two-photon probability distributions in all combinations of output modes. In contrast, two distinguishable photons will evolve independently and obey the statistics of Bernoulli trials. The corresponding output probability distribution $\Gamma^d_{k,l}$ takes the form

$$\Gamma^d_{k,l} = \frac{1}{1+\delta_{k,l}} \left(|U_{i,k}U_{j,l}|^2 + |U_{i,l}U_{j,k}|^2 \right). \tag{A.5}$$

In the case of photons and electromagnetic fields, $\Gamma^d_{k,l}$ represents an intensity correlation matrix $\Gamma^d_{k,l} = \langle I_k I_l \rangle$. The components $\Gamma^i_{k,l}$ and $\Gamma^d_{k,l}$ will differ by the factor $2\,\mathrm{Re}[(U_{i,k}U_{j,l}) * (U_{i,l}U_{j,k})]$, which encompasses the quantum nature of indistinguishable walkers.

To quantify the overlap fidelity between two probability distributions, we use $S = \left(\sum_{k,l} \sqrt{\Gamma_{k,l}\Gamma^p_{k,l}} \right)^2 / \sum_{k,l} \Gamma_{k,l} \sum_{k,l} \Gamma^p_{k,l}$ [27].

Mueller matrix

The Mueller-matrix array $\mathcal{M}$ describes the transfer properties of the circuit in terms of the Stokes parameters $\mathcal{S}$, which describe the polarization state of an electromagnetic field [29]. The component $M_{i,j}$ is the 4×4 Mueller matrix describing the coupling from input waveguide j to output waveguide i. From the corresponding output Stokes parameter $\mathcal{S}_{i,j}$ for the input state $|H\rangle_j$, the real-valued parameter $|U_{i,j}|^2$ was calculated as the output transmission component in the $|H\rangle_i$ subspace.

Table 1. Array $\mathcal{M}$ of 36 Mueller matrices, obtained from polarization-sensitive, coherent light tomography. This array fully describes the classical optical response of the waveguide array.

$$\{\mathcal{M}\} = \begin{pmatrix} M_{1,1} & \cdots & M_{1,6} \\ \vdots & \ddots & \vdots \\ M_{6,1} & \cdots & M_{6,6} \end{pmatrix}$$

$$= 10^{-2} \left(\begin{array}{cccc|cccc|cccc}
24.51 & -18.83 & -4.89 & -2.32 & 8.39 & 1.52 & 2.15 & 0.92 & 19.34 & -1.06 & 3.41 & -4.45 \\
-20.16 & 26.22 & 2.81 & -2.77 & 1.66 & 6.64 & 3.11 & 5.72 & 0.27 & 5.64 & -16.31 & -15.85 \\
2.42 & -3.57 & 8.18 & -19.65 & -0.35 & 3.54 & -7.40 & 0.01 & 3.63 & -18.81 & 4.39 & -11.81 \\
-7.69 & 5.84 & 21.04 & 9.23 & 0.89 & 5.15 & 2.64 & -6.68 & 5.19 & 11.15 & 16.31 & -14.00 \\
\hline
16.20 & 4.05 & 3.97 & 2.57 & 43.89 & 21.91 & -11.33 & 3.46 & 2.69 & 2.63 & 1.37 & -0.38 \\
1.88 & 15.38 & -5.17 & -4.88 & 26.78 & 42.58 & -19.28 & 9.28 & -1.81 & -1.79 & -1.57 & -0.91 \\
3.64 & 4.86 & -2.57 & 16.12 & 4.13 & -13.57 & -38.63 & 1.57 & -1.40 & -1.46 & 1.15 & -0.54 \\
-5.42 & -7.03 & -16.81 & -2.59 & 3.99 & 9.54 & -3.60 & -40.51 & 2.44 & 2.47 & 1.25 & -1.82 \\
\hline
7.77 & -6.72 & -1.85 & -5.82 & 0.37 & -0.32 & 0.10 & -0.11 & 43.51 & 1.17 & -13.56 & 19.12 \\
-0.55 & 1.04 & -3.43 & 0.26 & -0.07 & 0.05 & -0.14 & -0.24 & 5.88 & 40.78 & 13.23 & 19.07 \\
-6.18 & 5.17 & 1.57 & 6.45 & 0.26 & -0.29 & 0.14 & -0.25 & 5.52 & 21.04 & -38.14 & -18.28 \\
5.58 & -5.97 & -1.68 & -2.97 & -0.24 & 0.28 & 0.12 & -0.00 & -24.37 & 7.09 & 31.72 & -44.65 \\
\hline
9.13 & -9.07 & 1.64 & 0.46 & 35.91 & -17.89 & 6.16 & 0.90 & 0.66 & -0.46 & 0.22 & 0.26 \\
-9.79 & 9.85 & -2.04 & -0.60 & -20.32 & 37.74 & -3.79 & -7.64 & -0.33 & 0.33 & -0.71 & -0.21 \\
-1.75 & 1.73 & -0.06 & 0.37 & -1.21 & 9.61 & 9.90 & 30.06 & 0.36 & -0.62 & -0.04 & -0.38 \\
2.23 & -2.25 & 0.35 & 0.38 & -5.57 & 2.85 & -32.32 & 8.80 & -0.27 & 0.29 & 0.21 & -0.60 \\
\hline
0.81 & 0.17 & 1.37 & 1.28 & 0.02 & -0.00 & -0.00 & -0.00 & 27.88 & -1.34 & 12.54 & -12.09 \\
-0.55 & 0.15 & -1.22 & -1.06 & -0.01 & 0.00 & 0.01 & 0.00 & -1.19 & -10.62 & 13.42 & 19.06 \\
-0.58 & -0.43 & -1.09 & -1.11 & -0.02 & 0.00 & -0.00 & -0.00 & 6.81 & 21.63 & 15.27 & 0.45 \\
0.09 & 0.11 & 0.40 & -0.27 & -0.01 & 0.00 & -0.00 & 0.00 & 21.23 & -8.06 & 20.64 & -24.46 \\
\hline
41.59 & 30.40 & -0.25 & 3.82 & 11.42 & -5.21 & 2.92 & -5.18 & 5.93 & -0.95 & -3.98 & -2.46 \\
31.67 & 42.04 & -11.93 & -4.82 & -6.88 & 11.51 & -2.00 & 4.74 & -0.29 & 5.78 & -1.68 & 0.67 \\
15.52 & 18.13 & 18.27 & 29.85 & 0.92 & 1.55 & -7.65 & -8.68 & 3.44 & -0.41 & -4.24 & -5.92 \\
-1.09 & -7.70 & -31.63 & 21.38 & 2.74 & 1.48 & 9.46 & -7.52 & -1.65 & 1.94 & 5.68 & -1.64
\end{array} \right.$$

$$\left. \begin{array}{cccc|cccc|cccc}
3.03 & -1.47 & 4.15 & 2.16 & 8.89 & 2.42 & -2.92 & -1.04 & 33.34 & 9.02 & 1.30 & -1.14 \\
3.07 & -1.64 & 4.31 & 1.80 & 3.27 & 0.32 & -8.98 & 0.25 & 10.62 & 36.67 & -3.52 & -13.98 \\
1.49 & -0.49 & 2.46 & 1.69 & -1.63 & -8.39 & 0.23 & -3.15 & -0.45 & -12.27 & 10.14 & -33.96 \\
-0.70 & 0.86 & -0.42 & -0.72 & 2.83 & 3.86 & -1.24 & -8.62 & 6.28 & 8.66 & 34.62 & 9.51 \\
\hline
23.82 & -11.27 & 2.26 & 1.56 & 7.13 & -5.66 & 3.46 & -2.27 & 7.89 & 0.03 & 7.76 & 4.62 \\
-13.09 & 24.40 & -12.65 & -0.47 & -6.69 & 7.22 & -4.32 & 1.69 & -4.97 & -0.03 & -4.85 & -6.14 \\
-5.41 & 12.05 & 17.15 & -6.03 & 1.57 & -1.14 & -0.03 & -6.36 & 3.84 & -3.29 & 4.81 & 1.30 \\
0.02 & 4.93 & 3.60 & 21.42 & -1.27 & 2.74 & 4.66 & -0.22 & 5.71 & 2.44 & 6.35 & 2.06 \\
\hline
5.48 & -4.18 & 2.03 & -4.22 & 27.90 & 3.29 & 11.18 & -14.72 & 16.01 & 8.96 & -4.68 & -3.37 \\
-4.83 & 4.86 & -3.51 & 3.38 & -1.40 & -19.32 & -6.63 & -3.16 & 11.26 & 13.02 & -9.70 & -8.71 \\
2.91 & -2.95 & -2.07 & -3.76 & 10.11 & -5.61 & 21.89 & -2.05 & -4.27 & -11.34 & -0.86 & -11.26 \\
-0.16 & 1.61 & 2.32 & -3.66 & 21.39 & 6.04 & 6.75 & -27.47 & 2.42 & 6.42 & 12.54 & -6.51 \\
\hline
52.33 & 27.32 & -14.62 & 11.70 & 1.05 & -0.75 & 0.21 & 0.11 & 4.50 & -0.58 & -2.19 & 5.25 \\
35.12 & 48.38 & -10.62 & 27.49 & -0.72 & 0.88 & -0.62 & -0.33 & -1.46 & -1.52 & 2.65 & -2.40 \\
6.50 & -19.53 & -33.03 & 24.30 & -0.02 & -0.00 & 0.40 & -1.08 & 3.91 & -0.23 & -0.60 & 4.86 \\
11.26 & 16.57 & -30.93 & -30.44 & -0.51 & 0.80 & 0.68 & 0.30 & -1.99 & 2.33 & 2.64 & -2.59 \\
\hline
2.38 & -2.36 & -1.46 & -0.14 & 45.71 & -0.87 & -2.85 & 18.66 & 23.42 & -3.77 & 6.29 & -0.21 \\
2.05 & -2.07 & -0.05 & -0.55 & 11.35 & 37.49 & 0.79 & 29.00 & -5.40 & 12.39 & -13.28 & -20.14 \\
-1.33 & 1.32 & 1.62 & 0.62 & -1.24 & 9.25 & -45.50 & -11.73 & 4.17 & -22.51 & 1.89 & -12.93 \\
-1.40 & 1.39 & 0.95 & -1.49 & -19.88 & 25.77 & 18.00 & -42.56 & 6.30 & 7.07 & 21.99 & -9.18 \\
\hline
12.96 & -8.03 & 7.64 & -11.06 & 9.32 & 1.58 & -9.08 & -0.74 & 14.85 & -13.66 & -8.48 & -5.15 \\
-10.87 & 8.56 & -5.01 & 10.10 & 1.39 & 4.01 & -1.05 & 6.22 & -9.80 & 8.68 & 5.70 & 6.84 \\
9.70 & -4.73 & 7.89 & -9.01 & -7.07 & -3.77 & 9.20 & 3.09 & -14.07 & 13.53 & 8.84 & 3.71 \\
2.65 & -3.25 & 3.25 & 0.66 & 4.06 & -3.80 & -6.50 & 1.95 & 2.32 & -3.04 & 2.93 & -1.34
\end{array} \right).$$

Table 1 shows the calculated Mueller-matrix array $\mathcal{M}$ of the quantum walk circuit. The matrix not only allows us to determine the evolution matrix U in the $|H\rangle$ subspace, but also quantifies the polarization-dependent coupling and birefringence observed in the circuit, as seen in figure 4.

References

[1] Feynman R 1982 *Int. J. Theor. Phys.* **21** 467–88
[2] Lanyon B P *et al* 2010 *Nat. Chem.* **2** 106–11
[3] Du J, Xu N, Peng X, Wang P, Wu S and Lu D 2010 *Phys. Rev. Lett.* **104** 030502
[4] Lloyd S 1996 *Science* **273** 1073–8
[5] Aharonov Y, Davidovich L and Zagury N 1993 *Phys. Rev.* A **48** 1687
[6] Kempe J 2003 *Contemp. Phys.* **44** 307–27
[7] Mülken O and Blumen A 2011 arXiv:1101.2572
[8] Plenio M B and Huelga S F 2008 *New J. Phys.* **10** 113019
[9] Mohseni M, Rebentrost P, Lloyd S and Aspuru-Guzik A 2008 *J. Chem. Phys.* **129** 174106
[10] Karski M, Forster L, Choi J M, Steffen A, Alt W, Meschede D and Widera A 2009 *Science* **325** 174–7
[11] Zähringer F, Kirchmair G, Gerritsma R, Solano E, Blatt R and Roos C F 2010 *Phys. Rev. Lett.* **104** 100503
[12] Schmitz H, Matjeschk R, Schneider C, Glueckert J, Enderlein M, Huber T and Schaetz T 2009 *Phys. Rev. Lett.* **103** 090504
[13] Schreiber A, Cassemiro K N, Potoček V, Gábris A, Mosley P J, Andersson E, Jex I and Silberhorn C 2010 *Phys. Rev. Lett.* **104** 50502
[14] Broome M A, Fedrizzi A, Lanyon B P, Kassal I, Aspuru-Guzik A and White A G 2010 *Phys. Rev. Lett.* **104** 153602
[15] Farhi E and Gutmann S 1998 *Phys. Rev.* A **58** 915–28
[16] Bromberg Y, Lahini Y, Morandotti R and Silberberg Y 2009 *Phys. Rev. Lett.* **102** 253904
[17] Davis K M, Miura K, Sugimoto N and Hirao K 1996 *Opt. Lett.* **21** 1729–31
[18] Nolte S, Will M, Burghoff J and Tünnermann A 2003 *Appl. Phys.* A **77** 109–11
[19] Marshall G D, Politi A, Matthews J C F, Dekker P, Ams M, Withford M J and O'Brien J L 2009 *Opt. Express* **17** 12546–54
[20] Hein B and Tanner G 2009 *Phys. Rev. Lett.* **103** 260501
[21] Bulger D, Freckleton J and Twamley J 2008 *New J. Phys.* **10** 093014
[22] Kitagawa T, Rudner M, Berg E and Demler E 2010 *Phys. Rev.* A **82** 33429
[23] Szameit A, Dreisow F, Pertsch T, Nolte S and Tünnermann A 2007 *Opt. Express* **15** 1579–87
[24] Szameit A, Bloemer D, Burghoff J, Pertsch T, Nolte S and Tünnermann A 2006 *Appl. Phys. B: Lasers Opt.* **82** 507–12
[25] Keil R, Szameit A, Dreisow F, Heinrich M, Nolte S and Tünnermann A 2010 *Phys. Rev.* A **81** 23834
[26] Rohde P P, Schreiber A, Stefanak M, Jex I and Silberhorn C 2011 *New J. Phys.* **13** 013001
[27] Peruzzo A *et al* 2010 *Science* **329** 1500
[28] Minford W J, Korotky S K and Alferness R C 1982 *IEEE J. Quantum Electron.* **QE-18** 1802–6
[29] Hecht E and Zajac A 1974 *Optics* (Addison-Wesley)
[30] Hong C K, Ou Z Y and Mandel L 1987 *Phys. Rev. Lett.* **59** 2044–6
[31] Keil R, Dreisow F, Heinrich M, Tünnermann A, Nolte S and Szameit A 2011 *Phys. Rev.* A **83** 013808
[32] Pryde G J and White A G 2003 *Phys. Rev.* A **68** 052315
[33] Shabani A, Kosut R, Mohseni M, Rabitz H, Broome M, Almeida M, Fedrizzi A and White A 2009 arXiv:0910.5498
[34] Sansoni L, Sciarrino F, Vallone G, Mataloni P, Crespi A, Ramponi R and Osellame R 2010 *Phys. Rev. Lett.* **105** 200503